Chemically Encoded Self-Organized Quantum Chain Supracrystals with Exceptional Charge and Ion Transport Properties

Bo Hou[a,g,1], Myungbeom Sohn[b,1], Young-Woo Lee[c], Jingchao Zhang[d], Jung Inn Sohn[e], Hansu Kim[b,*], SeungNam Cha[a,f,*] and Jong Min Kim[g]

[a] Department of Engineering Science, University of Oxford, Parks Road, Oxford OX1 3PJ, U.K.
[b] Department of Energy Engineering, Hanyang University, 222, Wangsimni-ro, Seongdong-gu, Seoul, 04763, Republic of Korea
Email: khansu@hanyang.ac.kr
[c] Department of Energy Systems, Soonchunhyang University, Asan, Chungcheongnam-do 10 31538, Republic of Korea
[d] Holland Computing Centre, University of Nebraska-Lincoln, Lincoln, NE 68588, USA
[e] Division of Physics and Semiconductor Science, Dongguk University-Seoul, Seoul 100-715, 12 Republic of Korea
[f] Department of Physics, Sungkyunkwan University, Suwon, 16419, Republic of Korea
Email: chasn@skku.edu
[g] Department of Engineering, University of Cambridge, 9 JJ Thomson Avenue, Cambridge CB3 0FA, U.K.

[1]These authors contributed equally to this work

KEYWORDS

quantum dot, quantum chain, self-assembly, oriented-attachment, heterogeneous synthesis

ABSTRACT

Artificially grown superstructures from small building blocks is an intriguing subject in 'bottom-up' molecular science and nanotechnology. Although discrete nanoparticles with different morphologies and physicochemical properties are readily produced, assembly them into higher-order structure amenable to practical applications is still a considerable challenge. This report introduces a stepwise heterogeneous approach for coupling colloidal quantum dots (QDs) synthesis with self-organization to directly generate quantum chains (QCs). By using vulcanized sulfur precursors, QDs are interdigitated into microscale chainlike supracrystals associated with oleylamine and oleic acid as structure directing agents. The cooperative nature of the QD growth and assembly have been extended to fabricate binary (PbS) and ternary metal

chalcogenides ($CuInS_2$) QC superstructures over a range of length scales. In addition, enhanced ion and charge transfer performance have been demonstrated which are determined to originate from the minimum interparticle distance and nearly bare nanocrystal surface. The process reported here is general and can be readily extended to the production of many other metal chalcogenide QD superstructures for energy storage applications.

1. Introduction

Nanostructured materials lie at the forefront of the state of the art energy conversion and storage technologies because of their excellent mechanical and electrical properties.[1-8] Spontaneous assembly small building blocks into superstructures with distinct functionality are scientific challenges in fundamental science (e.g., the origin of life) and nanotechnologies.[9-12] Elaborately self-organized superstructures from low-dimensional materials could dramatically improve their optical-electrical properties as well as providing new collective phenomena through long-range ordered interparticle cross-linking.[12-16] For instance, the emergence of high mobility and conductivity QD solids have triggered tremendous frontier semiconductor studies, which map the progression from carrier hopping through localized quantum-confined states to band-like charge transport in delocalized and hybridized states.[15,17,18] Moreover, the preserved nanograin features such as abundant grain boundaries, absolute low volume changes that originate from the very small absolute size of the nanomaterials and high surface-to-volume ratio are the expected advantages for high-performance energy storage applications.[12,14,18-21]

Brownian colloidal nanocrystals can self-organize into superlattices through dynamically tailoring a range of accessible surface chemical ligands.[22] Generally, the self-assembly of pre-synthesized nanoparticles is reserved for building units which are not linked together *via* covalent bonds but through weak forces such as van der Waals or hydrogen bonding or even

hard particle interactions.[23] Bottom-up organization of nanocrystals with predefined functionality is often driven by both interparticle interactions and the influence of the assembly environment.[24] For instance, evaporation of carrier solvent, template-patterning, electric/magnetic fields inductions or fluid flow patterning are the main approaches for self-assembling colloidal nanocrystals into sophisticated superstructures.[15,16,25-27] However, self-assembled structures are prone to defects, and it is normally difficult to achieve a high degree of order that extends over large areas and quantities, which is the main challenge when assembled structures are to be integrated into devices.[17] One possible solution is to combine the colloidal self-assembly with other existing nanofabrication techniques, such as colloidal lithography. However, the particle size and the interparticle space are interdependent variables, thus cause them cannot be simply tailored with high patterning capability.[28,29] Recently, various molecules such as thiols, bipolar surfactants, ammonia sulfides or elemental sulfur have been used as effective linkers or reaction media to direct synthesis or connect nanoparticles during the initial synthesis process, meanwhile preserve their quantum confinement *via* the ligand substitution or cooperative growth/assembly process.[27,30-36] For example, metal oxide nanocrystals have been assembled into highly ordered superstructures using oleylamine (OLA) and oleic acid (OA) as capping and structure directing agents.[27] However, besides the metal oxide materials,[13,27,37] direct synthesis long-range ordered superstructures using metal sulfide as a building block, and their practical device applications, is still lacking within the community.

Here, we present a simple but effective approach to assemble QDs into one-dimensional (1D) quantum chain (QC) superstructure *via* a stepwise heterogeneous reaction approach. Using this method, high-quality lead sulfide (PbS) QDs can be rapidly crosslinked into microscale QCs through interdigitation of vulcanized solid sulfur precursors mediated by OLA and OA as structure directing agents. This growth method differs significantly from other reported self-

assembly methods because no new surfactant ligands or solvent evaporation are introduced, and the QC superstructure can be produced directly from the colloidal growth process. It is also confirmed that our growth strategy can be extended to the growth of other metal chalcogenides such as ternary copper indium sulfide ($CuInS_2$). We also demonstrate these chainlike structures can be readily applied to practical applications such as lithium-ion batteries (LIB). Owing to the minimum lattice stress from extremely small and adjacent crystal boundaries, QC-enabled LIB cells show a considerably higher electrochemical Li^+ storage capacity and charge mobility than discrete QDs and bulks.

2. Results and discussion

We extend the knowledge of homogeneous QD synthesis[3,37-42] to a heterogeneous reaction methodology, which enables an in situ rapid self-organization of QDs into chain-like superstructures. As illustrated in Fig 1a, isolated QDs firstly interacted with hexamethyldisilathiane (bis(trimethylsilyl) sulphide (TMS) to form bridged QDs as monomers.[30,31] OLA, OA subsequently provide nanoscale reactive vessels for bridged-QDs monomers to assembly into metastable mesostructures because the metal-surfactant complexes can be readily decomposed at high temperature through an ester elimination process.[43,44] In the end, QDs mesostructures are interdigitated by solid sulfur precursors through vulcanization reaction at elevated temperature, and self-organized into long order QC supercrystals.[7,34,35] Compared to previously reported works,[14,37,40] the as-obtained QCs not only maintain typical quantum-confined excitonic features but also exhibit a high synthesis yield with a micron dimension (Fig. 1b). The decrease of exciton peaks from QDs, bridged QDs to QCs could be revealed through absorption spectroscopy analysis (Fig. S1), which demonstrate enhanced necking and electronic coupling from long-range ordered QC superstructures.[5,6] Typical PbS rock-salt cubic crystalline structure[45] was determined by characteristic X-ray diffraction

(XRD) patterns and, as indexed in Fig. 1c, the attachment of these constituted QDs were found preferentially along the <100> axis with more than microns length scales (inset of Fig. 1c).

We carried out high-resolution transmission electron microscopy (TEM) and atomic-resolution microscopy (ARM) aberration-corrected high-angle annular dark-field scanning transmission electron microscopy (HAADF-STEM) analyses to understand detail morphology and microstructures of the as-prepared PbS QCs. False-color HAADF micrographs revealed that the PbS nanocrystals were well crystallized into monodispersed QDs (Fig. 2a), bridged QDs (Fig. S2a) and micron-length QCs (Fig. 2b). Fig. S2b, and Fig. S2c display the selected-area electron diffraction (SAED) patterns, which further manifest the embodied infinitesimal crystal domains in the characteristic broad and diffuse electron diffraction ring patterns.[46] Typical {111} and {200} lattice fringes can be resolved from the as-prepared PbS QDs (Fig. 2b), bridged QDs (Fig. S3) and QCs (Fig. 2c and Fig. 2d), which imply that the rock-salt cubic nanostructure is well preserved and independent from the shape transformation. Moreover, the HRTEM measurement provides additional evidence of the longitude attachment of QDs along the <200> direction embodied in the indexed spacing from {200} lattice fringes (i.e., 3.0±0.1 Å) presented in Fig. 2c, 2d, and Fig. S3.[35,45] Indeed, the bonding states of OA on the PbS QD surface is different between {111} and {200} planes. OA is just weakly adsorbed on {200} surface other than the coordinate bonded {111} planes.[8,47] Therefore, as shown in Figure 1a and Figure 2, through deliberately enriching the sulfur amount, populations of OA on {200} facets (i.e., S-rich QDs) will be reduced which result in the formation of one-dimensional structures via <200> oriented attachment.[45,48] The QCs provide a high number of grain boundaries and a large aspect ratio (e.g., width: length=1: 200) that are beneficial for charge transport and ion intercalation into the PbS lattice.[19,20,49] It has long been known that under ambient conditions, elemental sulfur primarily exists in a six to eight-membered ring form (S6-

S8) which melts at temperatures around 120°C and undergoes an equilibrium ring-opening polymerization of the S6-S8 monomer into a linear polysulfane with diradical chain ends, above 160°C.[34,50] Thereby, unsaturated metal sulfide species will tend to form new metal-S bonding to the adjacent particles to fulfill coordination numbers under the presence of these S_6-S_8 molecules.[30] As exhibited in Fig. 2c, Fig. S4, and Fig. S5, the QCs are composed of small polycrystalline nanograins with approximately 4-5 nm widths and micrometer lengths. The regular spacing of *ca.*1 nm (Fig. 2c and Fig.2d) separated each crystal along the length of the chain consistent with the presence of an interdigitated layer of S_6-S_8 sulfur molecules.[13,35,51,52] Further supporting this interpretation are the results through elemental X-ray photoelectron spectroscopy analysis (Fig. S6), which show the appearance of an S-rich feature consistent to the <200> attached PbS ensemble solids reported elsewhere.[45,48] Taken together, the S-rich stoichiometry indicates there are negligible Pb dangling bonds exist in QCs structure. However, solution-processed PbS QDs usually exhibits lead-rich characteristic[35,45], and excess Pb dangling bonds are normally passivated by initial, long-chain aliphatic ligands which are electronically insulated.[53] Therefore, as-proposed cross-linking of discrete QDs by sulfur molecules approach could also massively remove the bulky surfactant and enable the generation of nearly bare QD surface.[54,55] Notably, DNA-like double helix macromolecular structure is observed as shown in Fig. 2e which may generate from the side-to-side contact between the QCs to effectively decreases the interfacial energy.[3,27,56] These intriguing structures could provide interesting platforms for programmable constructing artificially chiral molecules in artificial protocell and biomimetic studies.[9-12]

We further employ a ternary Cu-In-S system to test this heterogeneous growth and assembly method. Significantly, $CuInS_2$ QDs (Fig. S7) and QC (Fig. 2f) nanostructures were prepared with uniform dimensions and morphologies. Fig. 2f, and Fig. S8 show the electron microscopy

images (HRTEM and HAADF-STEM) of as-synthesized uniform $CuInS_2$ QCs superstructures with the length of above *ca.* 100 nm. Moreover, HRTEM and HAADF-STEM energy-dispersive X-ray elemental mapping study further confirmed the highly crystalline and stoichiometric nature of these $CuInS_2$ QCs (Fig. S8).

To demonstrate that crosslinked QCs could facilitate a fast charge and ion transport associated with the enhanced kinetics of the electrode reaction and mass transfer process, we incorporated the as-prepared QDs and QCs as anode materials into benchmark LIB cells (inset of Fig. 3a). Butylamine (BAE) has been employed as a conductive ligand to enhance the charge transport properties of QDs and QCs (e.g., QDs@BAE, QCs@BAE) through in-situ solution-phase ligand-exchange.[57,58] Fig. S9a and Figure S9b display the morphologies of ligand-exchanged QDs and QCs samples (i.e., QDs@BAE and QCs@BAE). It can be seen that there is no significant structural variation after BAE ligand substitution.[59] As shown in the voltage profiles of the initial cycle (Fig. 3a, Fig. S9c, and Fig. S9d), the QCs@BAE electrodes exhibited higher initial discharge (i.e., delithiation) capacities (566.6 mAh g^{-1}) than the QDs@OA (274.5 mAh g^{-1}) and QDs@BAE (307.1 mAh g^{-1}); and this initial discharge capacity of QCs@BAE electrode is close to the Pb theoretical gravimetric capacity (~582 mAh g^{-1}) and far beyond the commercial graphite electrode (~372 mAh g^{-1}).[35,38,60,61] The electrochemical reactions of the electrodes during the lithiation and delithiation processes were probed by differential capacity plots (DCPs) and cyclic voltammetry (CV). In Fig. 3b and the inset, the DCPs extracted from the charge-discharge measurement (e.g., first cycle) show the electrochemical reactivity difference between QDs and QCs as a function of surface ligands and morphologies. For instance, the magnitudes of the oxidation peaks from the QCs@BAE electrodes are larger (~60 mV) than the rest of samples, which implies QCs@BAE electrodes hold better lithiation/delithiation sites and ion transport pathways than discrete QDs or bulk state.[49]

According to previous reports,[49,62,63] the CV and DCP peaks presented in Fig. 3b and Fig. S10 can be attributed to the conversion reaction of PbS into Li_2S and metallic Pb, followed by an alloying reaction of Pb with lithium:

$$PbS + (2/n)Li \longleftrightarrow Pb + (1/n)Li_2S_n \quad [1]$$

$$Pb + (1/n)Li_2S_n + (2-2/n)Li \longleftrightarrow Pb + Li_2S \quad [2]$$

$$Pb + 4.5Li + Li_2S \longleftrightarrow Li_{4.5}Pb + Li_2S \quad [3]$$

The redox currents observed at potentials greater than 1.0 V (vs. Li/Li^+) are attributed to the formation of lithium polysulfide (Li_xS, up to x=2) and metallic Pb (Equation 1).[49,64] The redox currents and CV peaks below 1.0 V might be highly related to the subsequent formation of Li-Pb alloy phases (Equation 2 and 3).[49,60,65] As highlighted in Fig. S10, two characteristic anodic CV peaks associated with the different amount of Li in the Li_yPb alloy can be resolved from the potential sweep.[65,66] Interestingly, compared to the bulk-state, the redox peaks corresponding to the formation of lithium polysulfide were not observed in our CV curves (Fig. S10), which may occur due to the QD-mediated fast Li diffusivity for promoting the Li_yPb alloy formation.[49,67] Notably, besides the higher current values from QCs@BAE (i.e., high charge mobility), no considerable redox potential difference between the QDs@OA and QDs@BAE electrodes was observed, which indicates that BAE ligand-exchange does not affect the lithium conversion mechanisms.

Electrochemical impedance spectroscopy (EIS) measurements were performed to understand the QC crosslinked framework in facilitating Li conversion and the charge transport kinetics. In Fig. 3c and Fig. 3d, EIS spectra for the electrodes, containing two consecutive semicircles with the linear region at low frequencies, are revealed after the first and fifth charge-discharge cycles.[68,69] The insets of Fig. 3c is referred to the equivalent circuit model used to fit the EIS experimental profiles.[70-72] In general, the high-frequency (HF) semicircle is related to solid

electrolyte interphase (SEI) formation process on the electrode material surface, and the mid-frequency (MF) semicircle reflects the impedance for the charge-transfer reaction at the interface between the electrolyte and the electrode material.[68,69] In Fig. 3c and d, the radii of both HF and MF semicircles in the QDs@OA anode are much larger than those in QDs@BAE and QCs@BAE, which reflects that the BAE ligand alleviates the impediments during Li transport through the PbS QD ensembles. We found that weaving QDs into micron-length QCs can further reduce the magnitude of the MF semicircle, which suggests that the proposed chain architecture improves the charge-transfer resistance between PbS and the electrolyte. This finding is also supported by the fitted EIS parameters listed in Table S1 as well as our theoretical calculations based on HSE06 hybrid density functional theory (Fig. S11). Indeed, the decreased resistance values in the QCs@BAE samples originated from the reduced interparticle distance and super-small crystal domains. For instance, in our DFT calculations (Fig. S11), the conductivity of the PbS QC increases dramatically at a short interparticle distance. As schematically illustrated in Fig. 3e and Fig. S11, synthetically, the LIB performance enhancement from the as-proposed QCs@BAE structure can be perceived as a synergistic effect associated with the QD microscopic crystal domains, and the QC crosslinked geometry: i) their ultra-small crystal domains have large surface areas that allow facile charging and discharging by shortening the diffusion length for Li-ion transport and high Li accessibility;[1,73,74] ii) the Li^+ diffusivities are ten times higher in the multiple grain boundary structures than in the continuing-lattice single crystals (e.g., the bulk state), as Li^+ diffuses by hopping between defects.[67] Therefore, the QC crosslinked textile framework is a preferred conducting medium for Li diffusional transport associated with disordered lattice structures from infinitesimal QDs and their enriched population of nanoscale boundaries.[67]

To demonstrate the QC nanostructure in improving the mechanical and reversible ion transport stability, we systematically investigated the cycle performance of the as-demonstrated LIBs. In Fig. 4a, our QCs@BAE electrode showed significantly stability improvement compared to discrete QDs (i.e., QDs@OA and QDs@BAE) and bulk due to the suppressed conversion/intercalation-induced stresses and crosslinked geometry.[49,67] For instance, the QCs@BAE discharge capacity monotonically increased after capacity degradation during the first few tens of cycles, which is different from the continuous capacity decrement reported in the bulk state.[49] Moreover, when the upper cut-off potential was set to 3.0 V, the discharge capacity of the QCs@BAE electrode reached 685 mAh g^{-1} at the 400th cycle, which is five times (489%) higher than the reported values from PbS bulk-state (e.g. 140 mA g^{-1} at the 100th cycle) and readily approach to its theoretical limit (i.e. 728 mAh g^{-1}).[49,60] In Fig. S12, the capacity retention of the PbS QDs and QCs electrode were over 100% at the 400th cycle, which is the best record among any reported Pb-based composite electrodes.[1,49,60,62] Due to the cross-linking of QDs in the QCs structure, the charge transfer between each QDs are primarily enhanced, which induce relatively smaller capacity retention of QCs compared to QDs samples. The average Coulombic efficiency (CE) of the QDs@BAE and QCs@BAE anodes was greater than 98% for over 400 cycles (Fig. 4b). Notably, the CE was enhanced after the ligand exchange, because the average CE of the QDs@BAE and QCs@BAE electrodes was approximately 98%, which is higher than that of the QDs@OA electrode (96%) over 200 cycles (Fig. S13). These findings suggest that the surface structure of QC anodes not only well preserved during cycling but also facilitate the alloying and dealloying reaction with lithium ions. Such promising electrochemical behavior may also be related to lithiation-induced reactivation, as observed in other metal chalcogenide materials,[9,75] because the preserved PbS rock-salt cubic is electrochemically active for lithium insertion, which can be reversibly transformed through a diffusionless process.[76]

Furthermore, the QCs@BAE cell was disassembled before (Fig. 4c) and after 400 cycles (Fig. 4d), and the segments were investigated by high-resolution TEM (HRTEM, Fig. S14) and HAADF-STEM microscopy. As illustrated in the high-resolution HAADF-STEM chemical mapping results (Fig. 4c, Fig. 4d and Fig. S15) and reconstructed electron-scatter amplitude-induced contrast images (Fig. S16), QCs@BAE can maintain its original nanoparticle features over 400 cycles, which suggests chainlike superstructure play a significant role as a buffer medium in suppressing the volume expansion of the Pb atoms.[63] It should be noted that the aggregation of nanocrystals is also observed which may be caused by the device preparation and the formation of SEI layers.[77] In Fig. 4e and Fig. S17, the crosslinked QCs@BAE framework also shows an enhanced rate capability compared to QD@BAE. Indeed, as rationalized in Fig. S18, the QC@BAE anode has a 226 mAh g^{-1} average discharge capability (at a current density of 3000 mA g^{-1}) which is 200% bigger than its bulk (e.g., 159 mAh g^{-1} at a current density of only 720 mA g^{-1}) and discrete QD states (e.g., 108 mAh g^{-1} at the current density of 3000 mA g^{-1}).[60] These findings indicate that QC superstructures hold great potential as a robust platform for reversible ion intercalation.

3. Conclusions

In summary, uniform metal chalcogenide nanocrystals with highly ordered QC superstructures were obtained using a stepwise heterogeneous growth approach. Through the interaction between surface ligands, sulfur molecules and inorganic species, well organized chain-like supracrystals can be formed. This simple synthetic method has been applied for the fabrication of binary and ternary metal chalcogenide QCs with micrometer dimensions which is not easily accessible with previously reported synthetic protocols. Meanwhile, novel collective properties from the assemblies of these QD building blocks have been systematically investigated through electrochemical charge and ion transfer analysis. As promising structure candidates for LIB,

QC structure possesses much better ion transport stability (above 400 cycles) and capacity compared to bulk (e.g., 500% times enhancement), and discrete-QD counterparts (e.g., 200% times enhancement). Additionally, through investigating the pre- and post-cycled LIBs by discerning the electrochemical reaction kinetics and the detailed microstructural variations, we confirmed the improved electrochemical capacity and durability were derived from the preserved nanograin boundaries and QC long-range crosslinked configuration. Such a novel superstructure represents a novel concept for the design of complicate nanostructure for high-performance energy storage applications, as well as open the door for other technologically important studies such as optoelectronics, photonics, and bionic science.

4. Experimental section

4.1. The growth of binary PbS QDs and bridged QDs

The synthesis of PbS QDs can be found in previous reports.[3,35,38,45] For the bridged PbS QDs, hexamethyldisilathiane (bis(trimethylsilyl) sulphide (TMS, 250 μL) was dissolved in ODE (6.4 mL) in a two-neck flask under vacuum. After 2 h, the TMS solution was switched to an Ar atmosphere at room temperature. The TMS solution was swiftly injected into the freshly prepared PbS QD solution, and the reaction flask was maintained at room temperature. The raw reaction solution was purified by adding a mixture of hexane and acetone, followed by centrifugation at 8000 rpm. Then, the nanocrystals were washed twice by dissolving in hexane and precipitating with ethanol (1/10, v/v). Finally, the bridged PbS QDs were dried into a powder for LIB device fabrication and subsequent QC formation.

4.2. The growth of binary PbS QC supracrystals

Fifty milligrams of the bridged PbS QDs were dispersed into 6 mL trioctylphosphine together with 1 mmol sulfur flakes and rapidly injected into a hot diphenyl ether (15 mL) solution that contained OLA (0.5 mL) and OA (2 mL) at 200 °C. After heating for 10 seconds, the reaction mixture was quenched to room temperature using a water bath. Then, the PbS QCs were

washed twice by dissolving in hexane and precipitating with ethanol (a vortex mixer was used for dispersing). Finally, the PbS QCs were dried into a powder for LIB device fabrication and characterization.

4.3. The growth of ternary $CuInS_2$ QDs and QC supracrystals

The synthesis of $CuInS_2$ QDs is adapted from previous reports.[50,59,77,78] For the synthesis of $CuInS_2$ QCs, fifty milligrams of the $CuInS_2$ QDs were dispersed into 6 mL trioctylphosphine together with 1 mmol sulfur flakes and rapidly injected into a hot diphenyl ether (15 mL) solution that contained OLA (0.5 mL) and OA (2 mL) at 200 °C. After heating for 10 seconds, the reaction mixture was quenched to room temperature using a water bath. Then, the $CuInS_2$ QCs were washed twice by dissolving in hexane and precipitating with ethanol (a vortex mixer was used for dispersing). Finally, the $CuInS_2$ QCs were dried into a powder for further characterizations.

4.4. In situ ligand exchange

The PbS-bridged QDs or QCs were dispersed in BAE and stirred under inert conditions for three days. The BAE dispersion was decanted into centrifuge tubes, and an excess amount of anhydrous isopropanol was added into the centrifuge tubes to precipitate the corresponding nanocrystals (40:1 isopropanol: BAE solution, v/v). Then, these solutions were centrifuged at 8000 rpm for 10 min. The supernatants were decanted, and the precipitated nanocrystals were dried into a powder for further utilization.

4.5. LIB fabrication

The battery fabrication was analogous to previous reports with some slight adjustments.[49,60] A slurry was made by mixing active materials (i.e., PbS QDs@OA, PbS QDs@BAE or PbS QCs@BAE), Super P as the conductive agent, and polyamide-imide (PAI) as the binder at a mass ratio of 6:2:2 in an N-methylpyrrolidone (NMP) solvent. The LIB anodes were fabricated by coating the slurry onto a 10-μm-thick copper foil and then were dried in a vacuum oven at

120 °C for 12 h. This electrode was punched into disks and assembled in an argon-filled glove box with Li metal foil as the counter electrode to form a 2032-type coin cell together with a porous polyethylene membrane (Celgard 2400 membrane) as the separator. A 1 M $LiPF_6$ solution dissolved in a mixed solvent of ethylene carbonate (EC) and diethyl carbonate (DEC) (1:1 v/v) was used as the electrolyte.

4.6. Electron microscopy analysis

Scanning transmission electron microscopy (STEM) and energy-dispersive X-ray spectroscopy (EDX) elemental mapping images were obtained by employing an atomic-resolution (ARM), aberration-corrected HAADF-STEM JEOL ARM-200F at 200 kV (cold field emission source, Cs probe corrected). The TEM, high-resolution transmission electron microscopy (HRTEM) and SAED images were captured by a JEOL JEM-3000F field emission gun TEM at 300 kV with a camera length of 255.8 mm.

4.7. LIB characterization

The CV and EIS measurements were performed using a VSP-300 potentiostat (Bio-Logic). The cycle performance was tested using coin cells on a battery testing system (BaSyTec Cell Test System) in a voltage range of 0.01-3 V vs. Li/Li^+ at a current density of 72.8 mAg^{-1}. The rate capability test was carried out in a voltage range of 0.01-3 V vs. Li/Li^+ at current densities of 150, 300, 1500, and 3000 mA g^{-1}.

4.8. Powder XRD and XPS

XRD analysis was carried out using a Bruker D8 Advance powder diffractometer employing Cu Kα radiation (λ=0.15406 nm) and an LYNXEYE XE detector. XPS analysis was performed on a Thermo Fisher Scientific K-Alpha XPS instrument equipped with a micro-focused monochromatic Al X-ray source. Data acquisition and analysis were performed with Thermo Scientific Advantage software. Peak fitting (Lorentzian/Gaussian (L/G) 30%) was applied following the removal of a Smart background. The normalized atomic percentages were

determined from the peak areas of the elemental central peaks detected on the survey scan following the background subtraction and application of thermosensitive factors.

Acknowledgements

This work was supported by the European Research Council (ERC Horizon2020 No. 685758), the Engineering and Physical Sciences Research Council (EPSRC, EP/P027628/1) and Basic Research Program through the National Research Foundation of Korea (NRF, MSIT-NRF-2017R1A2B2012847). B.H. would like to acknowledge EPSRC (EP/K040375/1) for funding the 'South of England Analytical Electron Microscope' used in this research.

Appendix A. Supporting information

Optical absorption spectra, advanced electron microscopy (TEM, HRTEM, SAED, HAADF-STEM, EDX Mapping), XPS analysis of QDs, bridged-QDs, QCs, and pre/post cycled LIB electrodes; charge/discharge capacities, coulombic efficiency, CV, DFT calculations of chainlike QDs, capacity retention, rate capability data; and fitting data from EIS spectroscopy; are provided in Fig. S1 to Fig. S18 and Table S1.

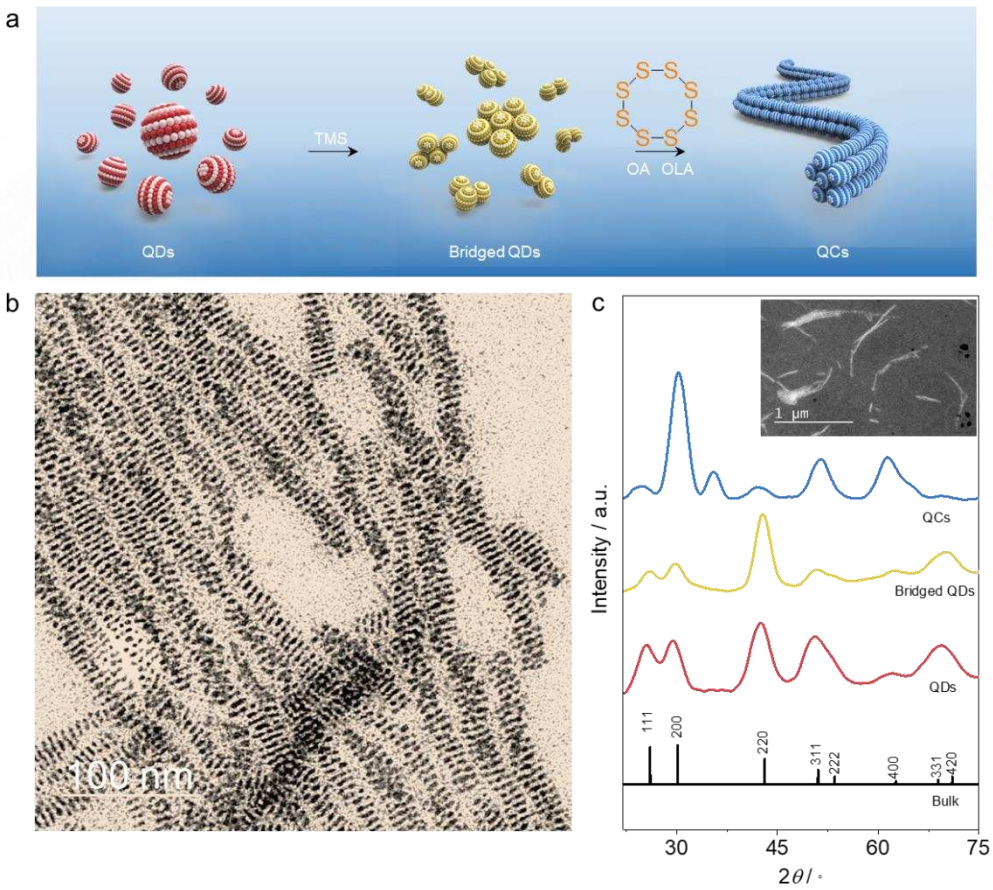

Fig. 1. a) A reaction scheme of the overall process for the spontaneous assembly QDs into QC supracrystals. b) TEM image showing ordered chains of PbS QCs. Scale bar = 100 nm. c) X-ray diffraction patterns of as-prepared PbS QDs, bridged QDs and QCs. Inset is the HAADF-STEM image of QCs. Scale bar = 1um.

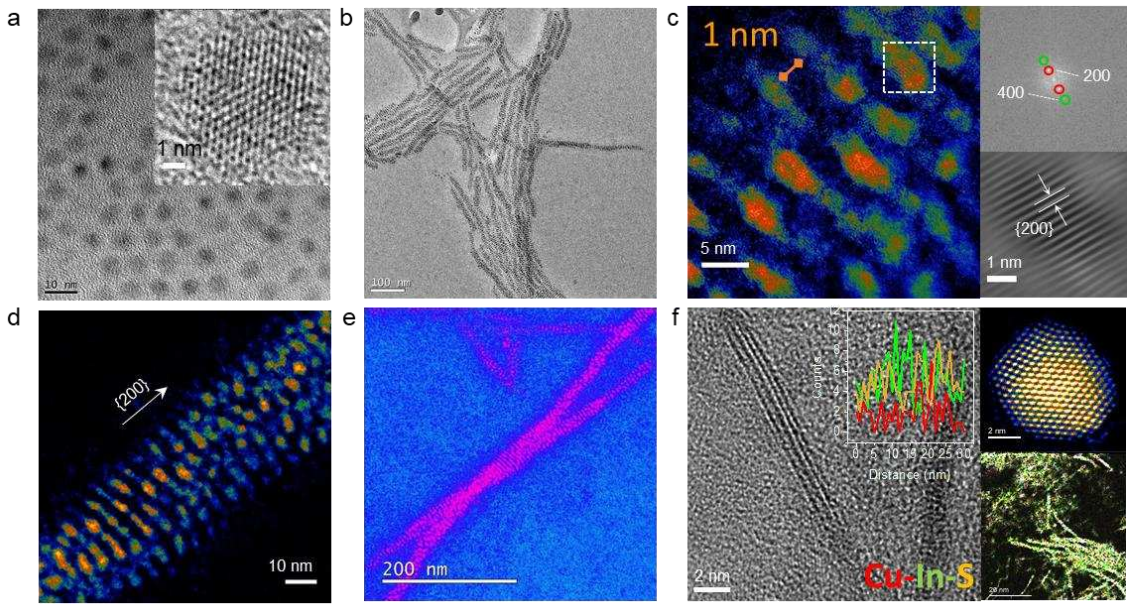

Fig. 2. a) TEM images of the as-prepared PbS QDs, scale bar = 10 nm. Inset is the HRTEM image taken from [001] zone axis, scale bar = 1 nm. b-d) ARM HAADF-STEM false color-scale images of the QCs, the insets of (c) are the fast Fourier transform nanopattern (top) and enlarged STEM image (bottom). e) Two QD chains that coil around each other to form a double helix DNA-like macromolecules. f) HRTEM (left panel) and ARM HAADF-STEM image and elemental mapping images of as-prepared $CuInS_2$ QDs (right top panel) and QCs (right bottom panel). The inset is the elemental profile line scan of QCs, and the scale bar in the HAADF-STEM images is 2 nm and 20 nm respectively.

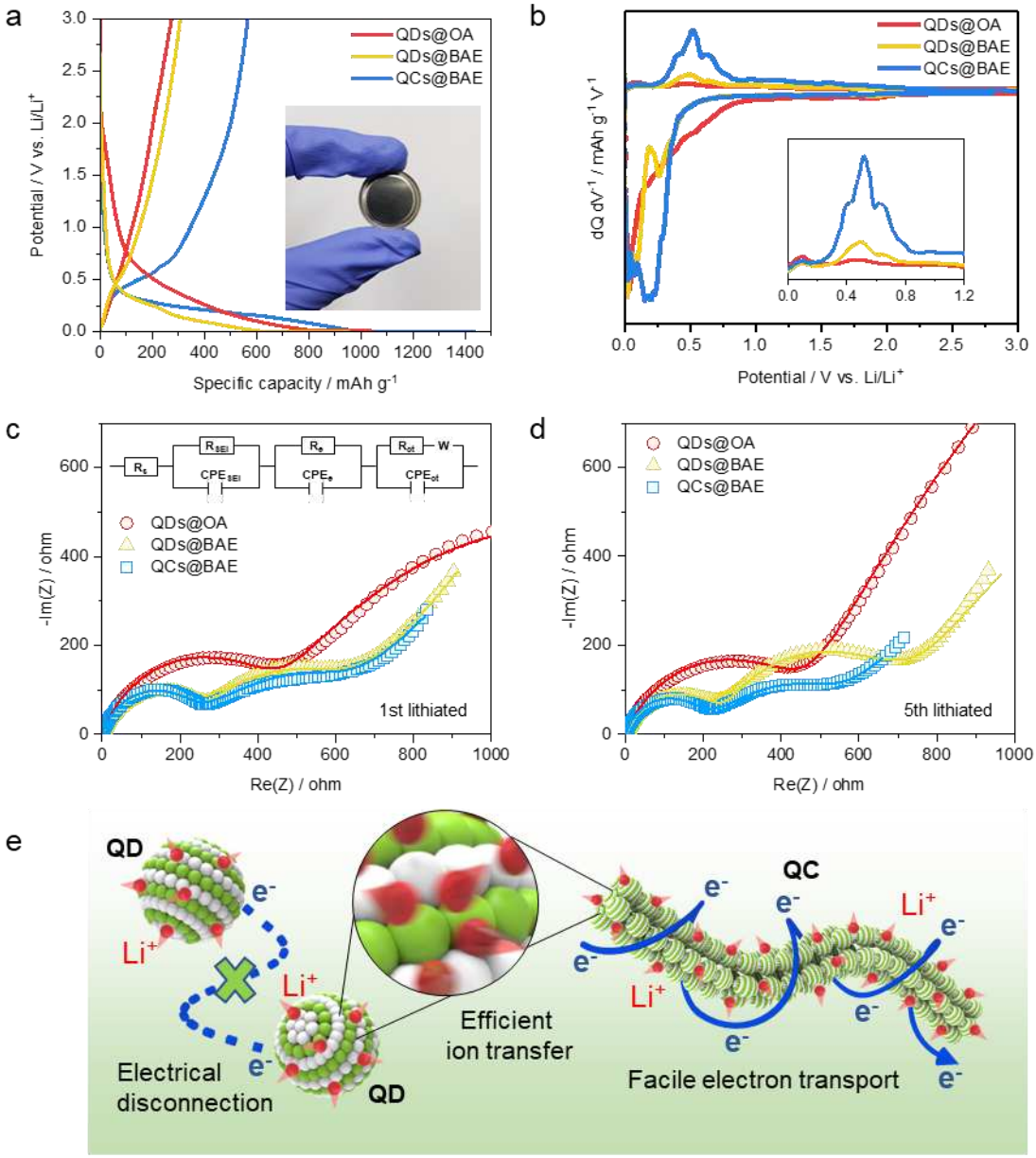

Fig. 3. Demonstrations of the QC-enabled LIB capacity enhancement and electrode reaction kinetics under different time domains. a) Voltage profiles and a photograph of as-prepared QC LIB cells and b) DCPs of the QDs@OA, QDs@BAE and QCs@BAE electrodes for the first cycle at 72.8 mAg^{-1} between 0.01–3 V. Nyquist plots of the first lithiated c) and fifth lithiated d) cycles on the QDs@OA, QDs@BAE, and QCs@BAE electrodes. e) Cross-section schematic shows the proposed charge and ion transport mechanisms in QC structure which enables facile charge propagation within QC and fast ion transfer through QDs domains.

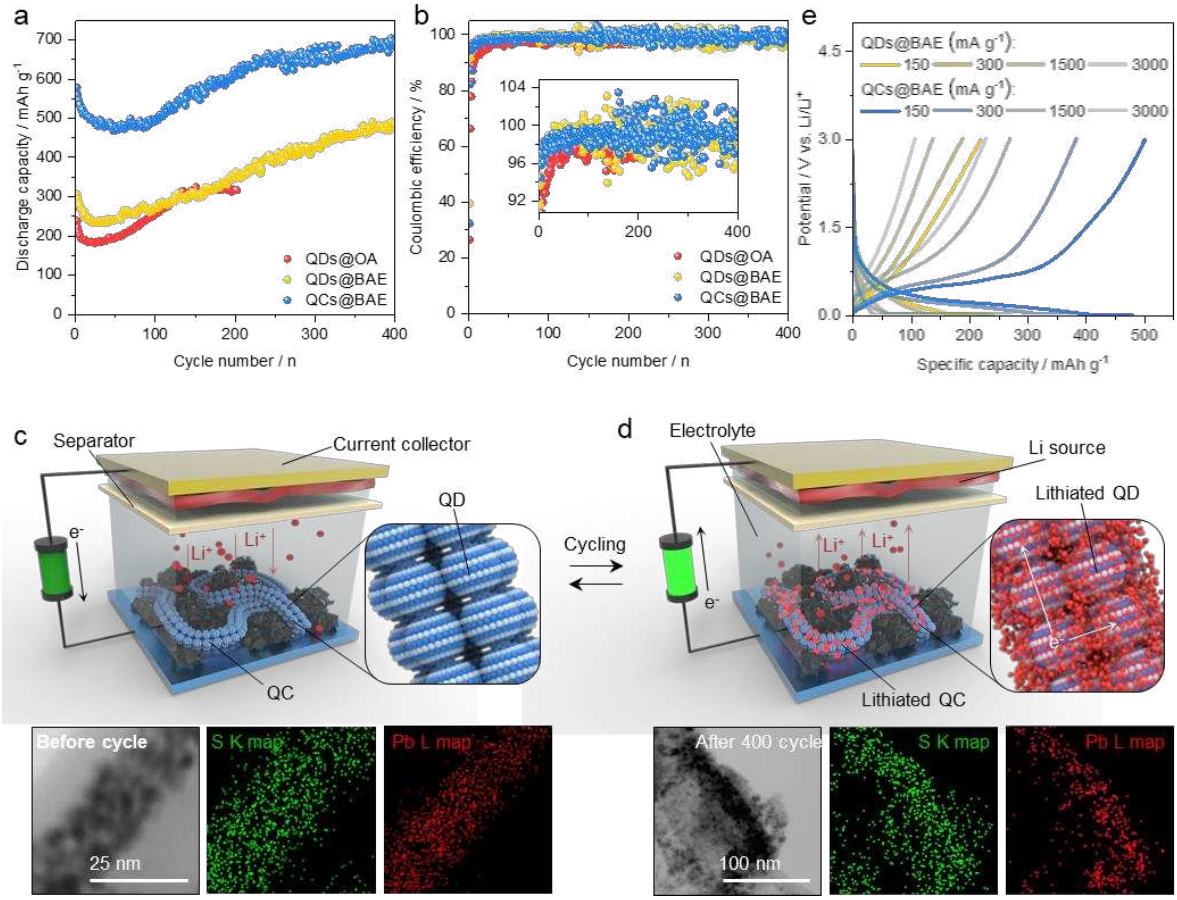

Fig. 4. a) Discharge capacity cycle performance and b) CE extracted from the QDs@OA, QDs@BAE and QCs@BAE electrodes. c, d) Schematic illustration and HAADF-STEM elemental mapping image of the QCs@BAE electrode segments before and after 400 cycles. e) Voltage profiles of QDs@BAE and QCs@BAE at current densities of 150, 300, 1500 and 3000 mA g^{-1}.

References

1. Nitta, N., Wu, F., Lee, J. T., Yushin, G., *Mater. Today* (2015) **18** (5), 252
2. Aricò, A. S., Bruce, P., Scrosati, B., Tarascon, J.-M., van Schalkwijk, W., *Nat. Mater* (2005) **4**, 366
3. Zhang, Horsch, M. A., Lamm, M. H., Glotzer, S. C., *Nano Lett.* (2003) **3** (10), 1341
4. Wang, Z., Wen, X.-D., Hoffmann, R., Son, J. S., Li, R., Fang, C.-C., Smilgies, D.-M., Hyeon, T., (2010) **107** (40), 17119
5. Stavrinadis, A., So, D., Konstantatos, G., *J. Phys. Chem. C* (2016) **120** (36), 20315
6. Kim, B.-S., Hong, J., Hou, B., Cho, Y., Sohn, J. I., Cha, S., Kim, J. M., *Applied Physics Letters* (2016) **109** (6), 063901
7. Hou, B., Benito-Alifonso, D., Kattan, N., Cherns, D., Galan, M. C., Fermín, D. J., *Chemistry – A European Journal* (2013) **19** (47), 15847
8. Zherebetskyy, D., Scheele, M., Zhang, Y., Bronstein, N., Thompson, C., Britt, D., Salmeron, M., Alivisatos, P., Wang, L.-W., *Science* (2014) **344** (6190), 1380
9. Sun, H., Xin, G., Hu, T., Yu, M., Shao, D., Sun, X., Lian, J., *Nat. Commun* (2014) **5**, 4526
10. Bonino, F., Morzilli, S., Scrosati, B., *J. Power Sources* (1985) **14** (1), 65
11. Martos, M., Morales, J., Sánchez, L., *Electrochim. Acta* (2003) **48** (6), 615
12. Penn, R. L., and Banfield, J. F., *Science* (1998) **281** (5379), 969
13. Li, M., Schnablegger, H., Mann, S., *Nature* (1999) **402**, 393
14. Tang, Z., Kotov, N. A., Giersig, M., *Science* (2002) **297** (5579), 237
15. Murray, C. B., Kagan, C. R., Bawendi, M. G., *Science* (1995) **270** (5240), 1335
16. Redl, F. X., Cho, K. S., Murray, C. B., O'Brien, S., *Nature* (2003) **423**, 968
17. Kagan, C. R., and Murray, C. B., *Nat. Nanotechnol* (2015) **10**, 1013
18. Kagan, C. R., Lifshitz, E., Sargent, E. H., Talapin, D. V., *Science* (2016) **353** (6302), aac5523
19. Kim, H., Lee, E.-J., Sun, Y.-K., *Mater. Today* (2014) **17** (6), 285
20. Kim, H., Jeong, G., Kim, Y.-U., Kim, J.-H., Park, C.-M., Sohn, H.-J., *Chem. Soc. Rev* (2013) **42** (23), 9011
21. Dai, C., Lim, J.-M., Wang, M., Hu, L., Chen, Y., Chen, Z., Chen, H., Bao, S.-J., Shen, B., Li, Y., Henkelman, G., Xu, M., *Adv. Funct. Mater.* (2018) **28** (14), 1704443
22. Boles, M. A., Engel, M., Talapin, D. V., *Chem. Rev* (2016) **116** (18), 11220
23. Min, Y., Akbulut, M., Kristiansen, K., Golan, Y., Israelachvili, J., *Nat. Mater* (2008) **7**, 527
24. Mann, S., *Angew. Chem. Int. Ed* (2013) **52** (1), 155
25. Deng, D., Hao, C., Sen, S., Xu, C., Král, P., Kotov, N. A., *J. Am. Chem. Soc* (2017) **139** (46), 16630
26. Whitham, K., Yang, J., Savitzky, B. H., Kourkoutis, L. F., Wise, F., Hanrath, T., *Nat. Mater* (2016) **15**, 557
27. Huo, Z., Tsung, C.-K., Huang, W., Fardy, M., Yan, R., Zhang, X., Li, Y., Yang, P., *Nano Lett.* (2009) **9** (3), 1260
28. Zhang, G., and Wang, D., *Chemistry – An Asian Journal* (2009) **4** (2), 236
29. Wood, M. A., *Journal of The Royal Society Interface* (2007) **4** (12), 1
30. Zhang, H., Hu, B., Sun, L., Hovden, R., Wise, F. W., Muller, D. A., Robinson, R. D., *Nano Lett.* (2011) **11** (12), 5356
31. Zhang, H., Yang, J., Chen, J.-R., Engstrom, J. R., Hanrath, T., Wise, F. W., *The Journal of Physical Chemistry Letters* (2016) **7** (4), 642
32. Andrew, A. R. W., David, B., Jamie, H. W., Elizabeth, A. T., Eric, L. T., Halina, R.-D., Paul, M., *Journal of Physics D: Applied Physics* (2005) **38** (12), 2006

33. Bear, J. C., Peveler, W. J., McNaughter, P. D., Parkin, I. P., O'Brien, P., Dunnill, C. W., *Chemical Communications* (2015) **51** (52), 10467
34. Chung, W. J., Griebel, J. J., Kim, E. T., Yoon, H., Simmonds, A. G., Ji, H. J., Dirlam, P. T., Glass, R. S., Wie, J. J., Nguyen, N. A., Guralnick, B. W., Park, J., Somogyi, Á., Theato, P., Mackay, M. E., Sung, Y.-E., Char, K., Pyun, J., *Nature Chemistry* (2013) **5**, 518
35. Hou, B., Cho, Y., Kim, B.-S., Ahn, D., Lee, S., Park, J. B., Lee, Y.-W., Hong, J., Im, H., Morris, S. M., Sohn, J. I., Cha, S., Kim, J. M., *J. Mater. Chem. C* (2017) **5** (15), 3692
36. Peng, X., *Acc. Chem. Res* (2010) **43** (11), 1387
37. Xia, Y., Nguyen, T. D., Yang, M., Lee, B., Santos, A., Podsiadlo, P., Tang, Z., Glotzer, S. C., Kotov, N. A., *Nat. Nanotechnol* (2011) **6**, 580
38. Hou, B., Cho, Y., Kim, B. S., Hong, J., Park, J. B., Ahn, S. J., Sohn, J. I., Cha, S., Kim, J. M., *ACS Energy Lett.* (2016) **1** (4), 834
39. Querejeta-Fernández, A., Hernández-Garrido, J. C., Yang, H., Zhou, Y., Varela, A., Parras, M., Calvino-Gámez, J. J., González-Calbet, J. M., Green, P. F., Kotov, N. A., *ACS Nano* (2012) **6** (5), 3800
40. Baumgardner, W. J., Whitham, K., Hanrath, T., *Nano Lett.* (2013) **13** (7), 3225
41. Cademartiri, L., Ghadimi, A., Ozin, G. A., *Acc. Chem. Res* (2008) **41** (12), 1820
42. Kim, J. Y., Voznyy, O., Zhitomirsky, D., Sargent, E. H., *Adv. Mater.* (2013) **25** (36), 4986
43. Cozzoli, P. D., Kornowski, A., Weller, H., *J. Am. Chem. Soc* (2003) **125** (47), 14539
44. Park, J., Joo, J., Kwon, S. G., Jang, Y., Hyeon, T., *Angew. Chem. Int. Ed.* (2007) **46** (25), 4630
45. Cho, K.-S., Talapin, D. V., Gaschler, W., Murray, C. B., *J. Am. Chem. Soc* (2005) **127** (19), 7140
46. Hou, B., Parker, D., Kissling, G. P., Jones, J. A., Cherns, D., Fermín, D. J., *J. Phys. Chem. C* (2013) **117** (13), 6814
47. Cao, Y., Stavrinadis, A., Lasanta, T., So, D., Konstantatos, G., *Nat. Energy* (2016) **1**, 16035
48. Bertolotti, F., Dirin, D. N., Ibáñez, M., Krumeich, F., Cervellino, A., Frison, R., Voznyy, O., Sargent, E. H., Kovalenko, M. V., Guagliardi, A., Masciocchi, N., *Nat. Mater* (2016) **15**, 987
49. Wood, S. M., Powell, E. J., Heller, A., Mullins, C. B., *J. Electrochem. Soc* (2015) **162** (7), A1182
50. Chung, W. J., Simmonds, A. G., Griebel, J. J., Kim, E. T., Suh, H. S., Shim, I.-B., Glass, R. S., Loy, D. A., Theato, P., Sung, Y.-E., Char, K., Pyun, J., *Angew. Chem. Int. Ed* (2011) **50** (48), 11409
51. Knop, O., Boyd, R. J., Choi, S. C., *J. Am. Chem. Soc* (1988) **110** (22), 7299
52. Hou, B., Benito-Alifonso, D., Webster, R., Cherns, D., Galan, M. C., Fermin, D. J., *J. Mater. Chem. A* (2014) **2** (19), 6879
53. Wang, R., Shang, Y., Kanjanaboos, P., Zhou, W., Ning, Z., Sargent, E. H., *Energy & Environmental Science* (2016) **9** (4), 1130
54. McPhail, M. R., and Weiss, E. A., *Chem. Mater* (2014) **26** (11), 3377
55. Oh, S. J., Berry, N. E., Choi, J.-H., Gaulding, E. A., Paik, T., Hong, S.-H., Murray, C. B., Kagan, C. R., *ACS Nano* (2013) **7** (3), 2413
56. Horsch, M. A., Zhang, Z., Glotzer, S. C., *Physical Review Letters* (2005) **95** (5), 056105
57. Konstantatos, G., Howard, I., Fischer, A., Hoogland, S., Clifford, J., Klem, E., Levina, L., Sargent, E. H., *Nature* (2006) **442**, 180
58. Saran, R., and Curry, R. J., *Nat. Photonics* (2016) **10**, 81
59. Clifford, J. P., Konstantatos, G., Johnston, K. W., Hoogland, S., Levina, L., Sargent, E. H., *Nat. Nanotechnol* (2008) **4**, 40

60. Wood, S. M., Klavetter, K. C., Heller, A., Mullins, C. B., *J. Mater. Chem. A* (2014) **2** (20), 7238
61. Grim, J. Q., Manna, L., Moreels, I., *Chem. Soc. Rev.* (2015) **44** (16), 5897
62. Wood, S. M., Pham, C. H., Heller, A., Mullins, C. B., *J. Electrochem. Soc* (2016) **163** (6), A1027
63. Lee, Y.-W., Kim, D.-M., Kim, S.-J., Kim, M.-C., Choe, H.-S., Lee, K.-H., Sohn, J. I., Cha, S. N., Kim, J. M., Park, K.-W., *ACS Appl. Mater. Interfaces* (2016) **8** (11), 7022
64. Cho, Y. J., Im, H. S., Kim, H. S., Myung, Y., Back, S. H., Lim, Y. R., Jung, C. S., Jang, D. M., Park, J., Cha, E. H., Cho, W. I., Shojaei, F., Kang, H. S., *ACS Nano* (2013) **7** (10), 9075
65. Huggins, R. A., *Journal of Power Sources* (1999) **81–82**, 13
66. Wang, J., King, P., Huggins, R. A., *Solid State Ion.* (1986) **20** (3), 185
67. Han, S., Park, J., Lu, W., Sastry, A. M., *J. Power Sources* (2013) **240**, 155
68. Wang, W., Favors, Z., Ionescu, R., Ye, R., Bay, H. H., Ozkan, M., Ozkan, C. S., *Sci. Rep* (2015) **5**, 8781
69. Guo, J., Sun, A., Chen, X., Wang, C., Manivannan, A., *Electrochim. Acta* (2011) **56** (11), 3981
70. Xu, S., Du, C., Xu, X., Han, G., Zuo, P., Cheng, X., Ma, Y., Yin, G., *Electrochim. Acta* (2017) **248**, 534
71. Huang, J., Li, Z., Ge, H., Zhang, J., *J. Electrochem. Soc* (2015) **162** (13), A7037
72. Osaka, T., Mukoyama, D., Nara, H., *J. Electrochem. Soc* (2015) **162** (14), A2529
73. Im, H. S., Cho, Y. J., Lim, Y. R., Jung, C. S., Jang, D. M., Park, J., Shojaei, F., Kang, H. S., *ACS Nano* (2013) **7** (12), 11103
74. Delacourt, C., Poizot, P., Levasseur, S., Masquelier, C., *Electrochem. Solid State Lett* (2006) **9** (7), A352
75. Yu, S.-H., Lee, S. H., Lee, D. J., Sung, Y.-E., Hyeon, T., *Small* (2016) **12** (16), 2146
76. Grimaud, A., *Nat. Energy* (2017) **2**, 17003
77. Son, I. H., Park, J. H., Park, S., Park, K., Han, S., Shin, J., Doo, S.-G., Hwang, Y., Chang, H., Choi, J. W., *Nat. Commun* (2017) **8** (1), 1561
78. Chen, B., Zhong, H., Zhang, W., Tan, Z. a., Li, Y., Yu, C., Zhai, T., Bando, Y., Yang, S., Zou, B., *Adv. Funct. Mater.* (2012) **22** (10), 2081